



LAWRENCE
LIVERMORE
NATIONAL
LABORATORY

Fe L-Shell Density Diagnostics in Theory and Practice

C. W. Mauche, D. A. Liedahl, K. B. Fournier

December 21, 2004

X-ray Diagnostics for Astrophysical Plasmas: Theory,
Experiment, and Observation
Cambridge, MA, United States
November 15, 2004 through November 17, 2004

Disclaimer

This document was prepared as an account of work sponsored by an agency of the United States Government. Neither the United States Government nor the University of California nor any of their employees, makes any warranty, express or implied, or assumes any legal liability or responsibility for the accuracy, completeness, or usefulness of any information, apparatus, product, or process disclosed, or represents that its use would not infringe privately owned rights. Reference herein to any specific commercial product, process, or service by trade name, trademark, manufacturer, or otherwise, does not necessarily constitute or imply its endorsement, recommendation, or favoring by the United States Government or the University of California. The views and opinions of authors expressed herein do not necessarily state or reflect those of the United States Government or the University of California, and shall not be used for advertising or product endorsement purposes.

Fe L-Shell Density Diagnostics in Theory and Practice

Christopher W. Mauche*, Duane A. Liedahl* and Kevin B. Fournier*

**Lawrence Livermore National Laboratory, L-473, 7000 East Avenue, Livermore, CA 94550*

Abstract.

We provide a discussion of the density and photoexcitation sensitivity of the X-ray spectra of Fe L-shell ions (Fe XVII–Fe XXIV) calculated with the Livermore X-ray Spectral Synthesizer, a suite of IDL codes that calculates spectral models of highly charged ions based primarily on HULLAC atomic data. These models are applicable to collisionally ionized laboratory or cosmic plasmas with electron temperatures $T_e \approx 2\text{--}45$ MK (0.2–4 keV) and electron densities $n_e \gtrsim 10^{11} \text{ cm}^{-3}$. Potentially useful density diagnostics are identified for Fe XVII and Fe XIX–Fe XXIII, with the most straightforward being the Fe XVII $I(17.10 \text{ \AA})/I(17.05 \text{ \AA})$ line ratio and the Fe XXII $I(11.92 \text{ \AA})/I(11.77 \text{ \AA})$ line ratio. Applying these models to the *Chandra* X-ray Observatory High Energy Transmission Grating spectrum of the intermediate polar EX Hya, we find that the strength of all the Fe L-shell lines are consistent with electron densities $n_e \gtrsim 1 \times 10^{14} \text{ cm}^{-3}$. Specifically, from the observed Fe XVII $I(17.10 \text{ \AA})/I(17.05 \text{ \AA})$ line ratio, we infer an electron density $n_e \gtrsim 2 \times 10^{14} \text{ cm}^{-3}$ at the 3σ level, while from the observed Fe XXII $I(11.92 \text{ \AA})/I(11.77 \text{ \AA})$ line ratio, we infer $n_e = 1.0^{+2.0}_{-0.5} \times 10^{14} \text{ cm}^{-3}$ at the 1σ level and $n_e \gtrsim 2 \times 10^{13} \text{ cm}^{-3}$ at the 3σ level.

Keywords: atomic processes — binaries: close — stars: individual (EX Hydrae) — stars: magnetic fields — X-rays: binaries

PACS: 32.30.Rj, 97.80.Gm

INTRODUCTION

The standard density diagnostic of high-temperature plasmas is the intensity ratio $R \equiv f/i$ of the forbidden to intercombination lines of He-like ions, which falls from its low-density value R_0 to zero at a critical density (where $R/R_0 = 0.5$) that increases from $n_e \approx 3 \times 10^8 \text{ cm}^{-3}$ for C to $n_e \approx 3 \times 10^{17} \text{ cm}^{-3}$ for Fe [16, 4, 36, 37] (see left panel of Fig 1). Unfortunately, this diagnostic is compromised in ultraviolet-bright sources like O stars and cataclysmic variables, wherein photoexcitation competes with collisional excitation to depopulate the upper level of the forbidden line, causing the R line ratio to appear to be in the high-density limit regardless of the density; for a plasma illuminated by a 30 kK blackbody, this is true for all elements through Mg [27] (see right panel of Fig 1). In an attempt to circumvent this problem, we have undertaken an investigation of potential density diagnostics of lines of Fe L-shell ions (Fe XVII–Fe XXIV). These diagnostics are applicable to collisionally ionized plasmas with electron temperatures $T_e \approx 2\text{--}45$ MK (0.2–4 keV) and electron densities $n_e \gtrsim 10^{11} \text{ cm}^{-3}$. Given the high densities, these diagnostics are particularly suitable to magnetic cataclysmic variables (polars and intermediate polars [41]), in which the density of the X-ray-emitting plasma is increased by (1) the magnetic channeling of the mass lost by the secondary onto small

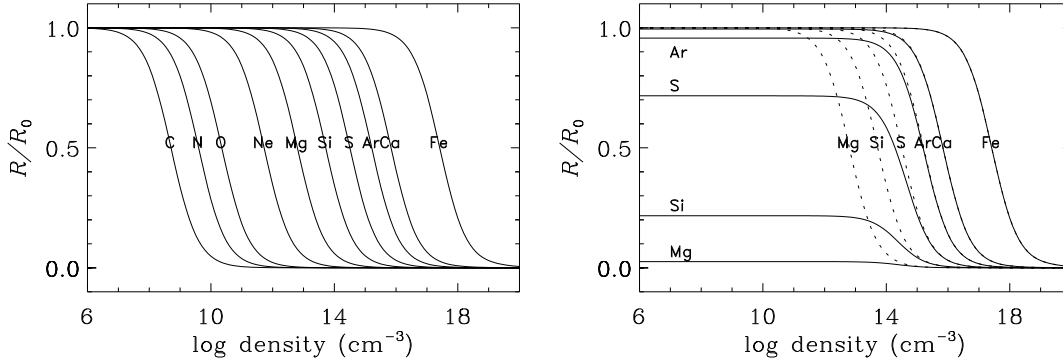


FIGURE 1. *Left panel:* He-like $R \equiv z/(x+y) = f/i$ line ratios of the abundant elements as a function of electron density. For C, N, O, ..., Fe, the plasma temperatures $T_e = 0.46, 0.57, 0.86, \dots, 36.1$ MK, the temperature of the peak ionization fraction for each ion [30]. *Right panel:* Similar to the left panel (*dotted curves*), but accounts for photoexcitation by a $T_{bb} = 30$ kK blackbody (*full curves*). In both panels the line ratios are scaled to the low-density limit R_0 for ease of comparison.

spots near the white dwarf magnetic poles; (2) the factor-of-four density jump across the standoff shock, which heats the plasma to a temperature $T_s = 3GM_{wd}\mu m_H/8kR_{wd} \approx 200$ MK; and (3) the settling nature of the post-shock flow, wherein the pressure is roughly constant and the density scales inversely with the decreasing temperature [12]. For a mass-accretion rate $\dot{M} = 10^{15} \text{ g s}^{-1}$ (hence luminosity $L = GM_{wd}\dot{M}/R_{wd} \approx 6 \times 10^{31} \text{ erg s}^{-1}$), a free-fall velocity $v_{ff} = (2GM_{wd}/R_{wd})^{1/2} \approx 3600 \text{ km s}^{-1}$, and a relative spot size $f = 0.1$, the density of the accretion flow immediately behind the shock $n = \dot{M}/4\pi f R_{wd}^2 \mu m_H (v_{ff}/4) \approx 10^{13} \text{ cm}^{-3}$.

In two previous publications, we explored the density and photoexcitation sensitivity of the Fe XVII $I(17.10 \text{ \AA})/I(17.05 \text{ \AA})$ line ratio [28] and the Fe XXII $I(11.92 \text{ \AA})/I(11.77 \text{ \AA})$ line ratio [29] and applied them to the *Chandra* X-ray Observatory High-Energy Transmission Grating Spectrometer (HETGS) Medium Energy Grating (MEG) spectrum of the intermediate polar EX Hya [17, 19, 15, 10, 18]. We summarize the results of those investigations below, but first provide a general look at the *Chandra* HETG spectrum of EX Hya and the density sensitivity of the X-ray spectra of all Fe L-shell ions.

CHANDRA SPECTRUM OF EX HYA

We begin by comparing the *Chandra* MEG spectrum of EX Hya with that of the coronally active RS CVn binary HR 1099 [1, 31, 32]. As one of the targets of the *Chandra* Emission Line Project (<http://asc.harvard.edu/elp/ELP.html>) [5], HR 1099 was observed extensively by *Chandra*, and its X-ray spectrum is one of the benchmarks for models of collisionally ionized plasmas. Figure 2 shows the MEG count spectra of EX Hya (*blue histogram*) and HR 1099 (*red histogram*) in the 10.5–17.5 Å bandpass, which contains the strongest lines of Fe L-shell ions. The spectrum of EX Hya differs from that of HR 1099 in (1) the absence of the Fe XVII 17.10 Å line, (2) the strength of the Fe XVII 17.05 Å line, (3) the absence of the Ne IX 13.70 Å forbidden

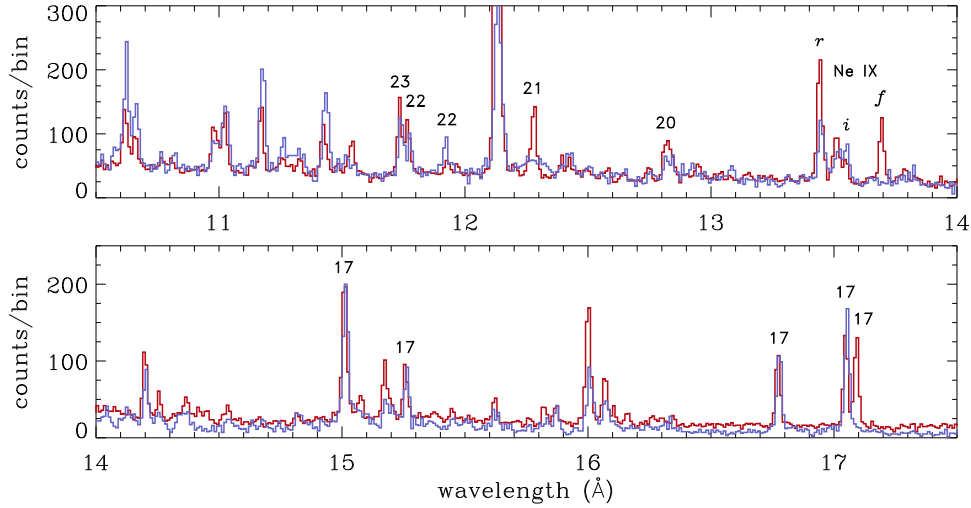


FIGURE 2. *Chandra* MEG count spectra (combining ± 1 st orders and binned to 0.005 \AA) of EX Hya (blue histogram) and HR1099 (red histogram). The HR 1099 data is scaled by a factor of 0.25 in the upper panel and 0.34 in the lower panel, and the Ne IX and Fe L-shell lines discussed in the text are labeled.

line, (4) the weakness of the Fe XX 12.83 \AA line, (5) the absence of the Fe XXI 12.26 \AA line, and (6) the strength of the Fe XXII 11.92 \AA line. As shown by Fig 1, the absence of the Ne IX forbidden line is indicative of electron densities $n_e \gtrsim 1 \times 10^{13} \text{ cm}^{-3}$ or of photoexcitation by a $T_{\text{bb}} \gtrsim 30 \text{ kK}$ blackbody. The later possibility cannot be excluded in EX Hya, whose far ultraviolet spectrum has been modeled as a $T_{\text{bb}} \approx 25 \text{ kK}$ white dwarf [17] and as a $T_{\text{bb}} \approx 20 \text{ kK}$ white dwarf with a $T_{\text{bb}} \approx 37 \text{ kK}$ hotspot [26]. As we will see below, the Fe XVII $I(17.10 \text{ \AA})/I(17.05 \text{ \AA})$ line ratio and the Fe XXII $I(11.92 \text{ \AA})/I(11.77 \text{ \AA})$ line ratio are less sensitive to photoexcitation, and indeed the strength of all the Fe L-shell lines are consistent with electron densities $n_e \gtrsim 1 \times 10^{14} \text{ cm}^{-3}$.

LXSS FE L-SHELL MODEL SPECTRA

We constructed model spectra of Fe L-shell ions using the Livermore X-ray Spectral Synthesizer (LXSS), a suite of IDL codes that calculates spectral models of highly charged ions based on Hebrew University/Lawrence Livermore Atomic Code (HULLAC) atomic data. HULLAC calculates atomic wavefunctions, level energies, radiative transition rates, and oscillator strengths according to the fully relativistic, multiconfiguration, parametric potential method [21, 22]. Electron impact excitation rate coefficients are computed quasi-relativistically in the distorted wave approximation [2] assuming a Maxwellian velocity distribution. Table 1 lists the number of energy levels, radiative transition rates for E1, E2, M1, and M2 decays, and electron impact excitation rate coefficients for each of our Fe L-shell models. Using these data, LXSS calculates the level populations for a given temperature and density assuming collisional-radiative equilibrium. The line intensities are then simply the product of the level populations and the radiative transition rates. In the sections below on Fe XVII and Fe XXII, we account for

TABLE 1. LXSS Fe L-shell Models

Ion	Levels	Collisional Rates	Radiative Rates
Fe XVII	281	33,887	49,882
Fe XVIII	456	93,583	141,229
Fe XIX	605	164,496	240,948
Fe XX	609	165,350	257,765
Fe XXI	591	153,953	227,743
Fe XXII	228	24,084	37,300
Fe XXIII	116	6,478	8,798
Fe XXIV	76	1,704	4,100

photoexcitation by including in the LXSS population kinetics calculation the photoexcitation rates $(\pi e^2/m_e c) f_{ij} F_V(T)$, where $F_V(T)$ is the continuum spectral energy distribution and f_{ij} are the oscillator strengths of the various transitions. For simplicity, we assume that $F_V(T) = (4\pi/h\nu) B_V(T_{\text{bb}})$ (i.e., the radiation field is that of a blackbody of temperature T_{bb}) and the dilution factor of the radiation field is equal to $\frac{1}{2}$ (i.e., the X-ray emitting plasma is in close proximity to the source of the photoexcitation continuum).

The resulting Fe L-shell ion spectra are shown in Figs 3–6. In each case, the atomic model was calculated at the temperature of the peak ionization fraction for each ion [30] for electron densities $n_e = 10^{10}$ – 10^{18} cm^{-3} , and the spectra were binned to 0.02 Å, which is approximately equal to the FWHM of the MEG spectra. The upper and lower panels of each figure show the model spectra at the extremes of the density grid: $n_e = 10^{10}$ cm^{-3} in red and $n_e = 10^{18}$ cm^{-3} in blue. Note that each panel encompasses a different 4 Å bandpass, allowing them to be compared directly to Fig 2. In each case, the spectrum is scaled to the brightest line in the $n_e = 10^{10}$ cm^{-3} model and by a factor of $(10^{10} \text{ cm}^{-3})/n_e$. The middle panels of each figure show as a function of electron density the relative line strengths for lines brighter than 0.25 photons/bin. Each of these models is discussed in turn.

Fe XVII: The X-ray spectrum of Ne-like Fe XVII is dominated at low densities by the three $3d$ – $2p$ lines near 15 Å and the three $3s$ – $2p$ lines near 17 Å. As the density increases, the 17.10 Å line disappears and the 17.05 Å line brightens. As shown below, the $I(17.10 \text{ Å})/I(17.05 \text{ Å})$ line ratio observed in EX Hya is consistent with $n_e \gtrsim 2 \times 10^{14} \text{ cm}^{-3}$ at $T_e \approx 4.1$ MK.

Fe XVIII: The X-ray spectrum of F-like Fe XVIII is dominated at low densities by the $3d$ – $2p$ line at 14.20 Å. As the density increases, the three brightest lines of this ion all dim, providing no useful density diagnostic.

Fe XIX: The X-ray spectrum of O-like Fe XIX is dominated at low densities by a tight clump of $3d$ – $2p$ lines near 13.5 Å. As the density increases, the 13.52 Å and 13.50 Å lines dim and the 13.48 Å line brightens, providing a potential density diagnostic, although these lines are blended with the (typically brighter) He α lines of Ne IX.

Fe XX: The X-ray spectrum of N-like Fe XX is dominated at low densities by a broad clump of $3d$ – $2p$ lines near 12.8 Å. As the density increases, the 12.80 Å and 12.82 Å lines dim and the 12.86 Å, 12.96 Å, and 12.90 Å lines brighten, providing a potential

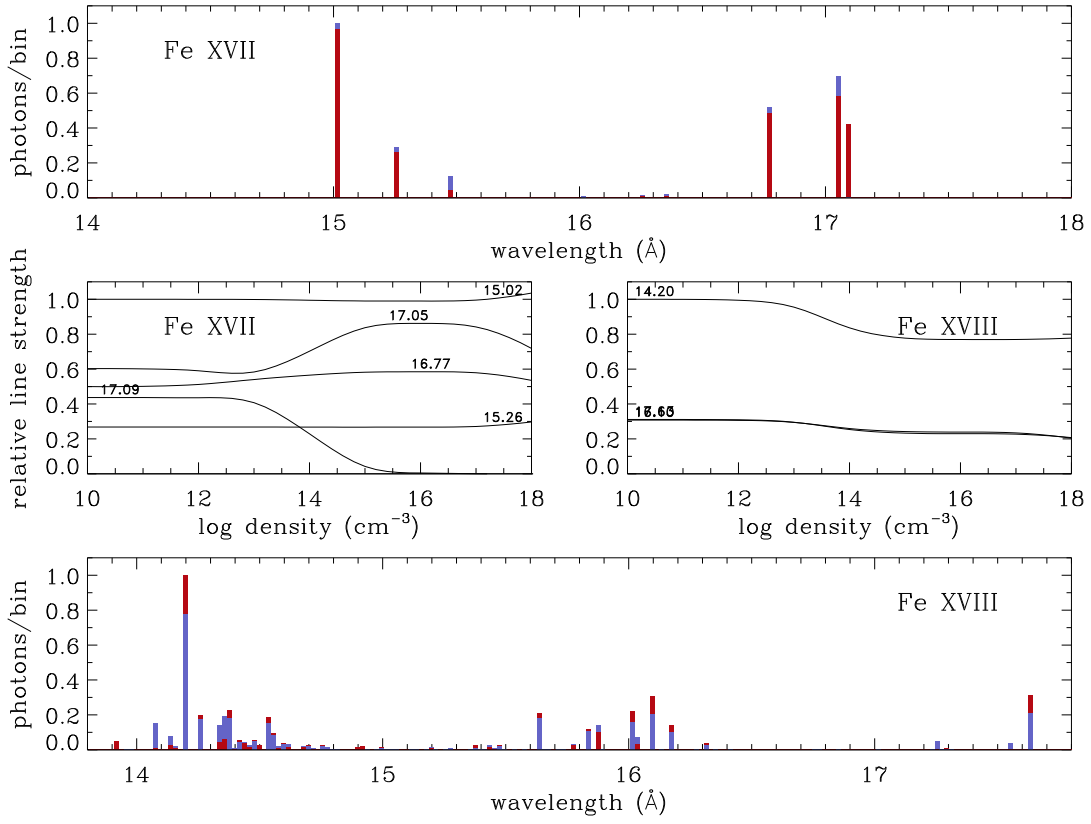


FIGURE 3. LXSS models of Fe XVII at $T_e = 4.1$ MK and Fe XVIII at $T_e = 6.6$ MK. Upper and lower panels show the model spectra binned to 0.02 \AA for $n_e = 10^{10} \text{ cm}^{-3}$ (red bars) and $n_e = 10^{18} \text{ cm}^{-3}$ (blue bars); middle panels show as a function of electron density the relative line strengths for lines brighter than 0.25 photons/bin.

density diagnostic. The weakness of the 12.8 \AA line in EX Hya is consistent with $n_e \gtrsim 3 \times 10^{14} \text{ cm}^{-3}$ at $T_e \approx 9.5$ MK.

Fe XXI: The relatively simple X-ray spectrum of C-like Fe XXI is dominated at low densities by a single $3d-2p$ line at 12.26 \AA . As the density increases, this line dims and the 12.38 \AA line brightens, providing a potential density diagnostic. The absence of the 12.26 \AA line in EX Hya is consistent with $n_e \gtrsim 3 \times 10^{13} \text{ cm}^{-3}$ at $T_e \approx 10.5$ MK.

Fe XXII: The X-ray spectrum of B-like Fe XXII is dominated at low densities by the $3d_{3/2}-2p_{1/2}$ line at 11.77 \AA . As the density increases, this line dims and the $3d_{5/2}-2p_{3/2}$ line at 11.92 \AA line brightens, providing a clear density diagnostic. As shown below, the $I(11.92 \text{ \AA})/I(11.77 \text{ \AA})$ line ratio observed in EX Hya is consistent $n_e \approx 1 \times 10^{14} \text{ cm}^{-3}$ at $T_e \approx 12.3$ MK.

Fe XXIII: The X-ray spectrum of Be-like Fe XXIII consists of a few strong $3d-2p$ lines between $11.0-12.2 \text{ \AA}$. As the densities increases, the 11.74 \AA line dims and the 11.44 \AA line brightens, but they do not become comparable in strength until $n_e \approx 10^{18} \text{ cm}^{-3}$.

Fe XXIV: The X-ray spectrum of Li-like Fe XXIV consists of a few strong $3s-2p$, $3d-2p$, and $3p-2s$ lines between $10.6-11.4 \text{ \AA}$. There is little density dependence to its X-ray

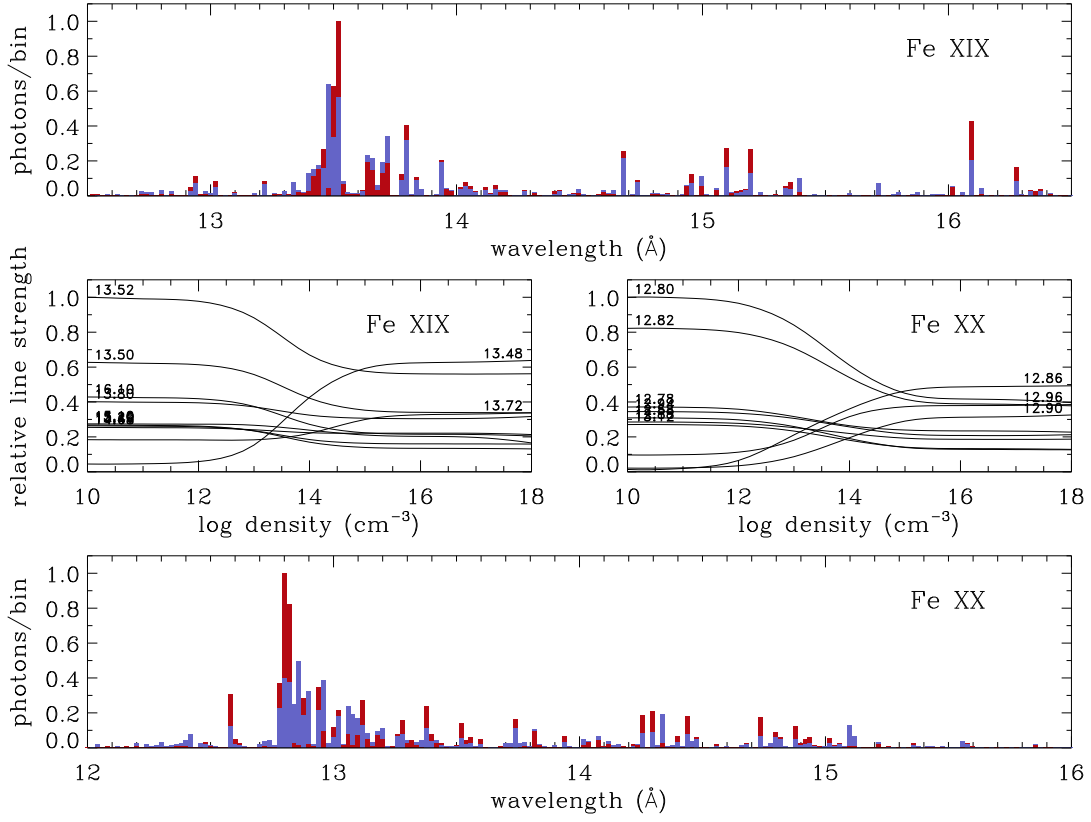


FIGURE 4. Similar to Fig 2, for Fe XIX at $T_e = 7.9$ MK and Fe XX at $T_e = 9.5$ MK.

spectrum.

Based on the foregoing, it is clear that the Fe XVII $I(17.10 \text{ \AA})/I(17.05 \text{ \AA})$ line ratio and the Fe XXII $I(11.92 \text{ \AA})/I(11.77 \text{ \AA})$ line ratio provide the most straightforward density diagnostics of Fe L-shell ions. Each of these is discussed in more detail below.

FE XVII

Because of the persistence of Ne-like Fe XVII over a broad temperature range ($T_e \approx 2\text{--}12$ MK) and the large collision strengths for $2p \rightarrow nd$ transitions, the $2p^6\text{--}2p^53l$ ($l = s, d$) lines of Fe XVII at $15\text{--}17 \text{ \AA}$ are prominent in the X-ray spectra of high-temperature plasmas in tokamaks [23, 35, 3], the Sun [38, 35, 39], and both late- and early-type stars [6, 1, 20, 40]. The lowest-lying configurations of Fe XVII are the $2p^6$ ground state, the $2p^53s$ manifold (4 levels), the $2p^53p$ manifold (10 levels), and the $2p^53d$ manifold (12 levels) (Fig 7). Because electron impact excitation from the ground state is strong for transitions into the $2p^5nd$ configurations, but weak for transitions into the $2p^53s$ configuration, the population flux into the lowest-lying configuration is dominated by radiative cascades originating on higher-lying energy levels, rather than direct excitation from the ground state [24]. The four levels of the $2p^53s$ configuration have, in increasing

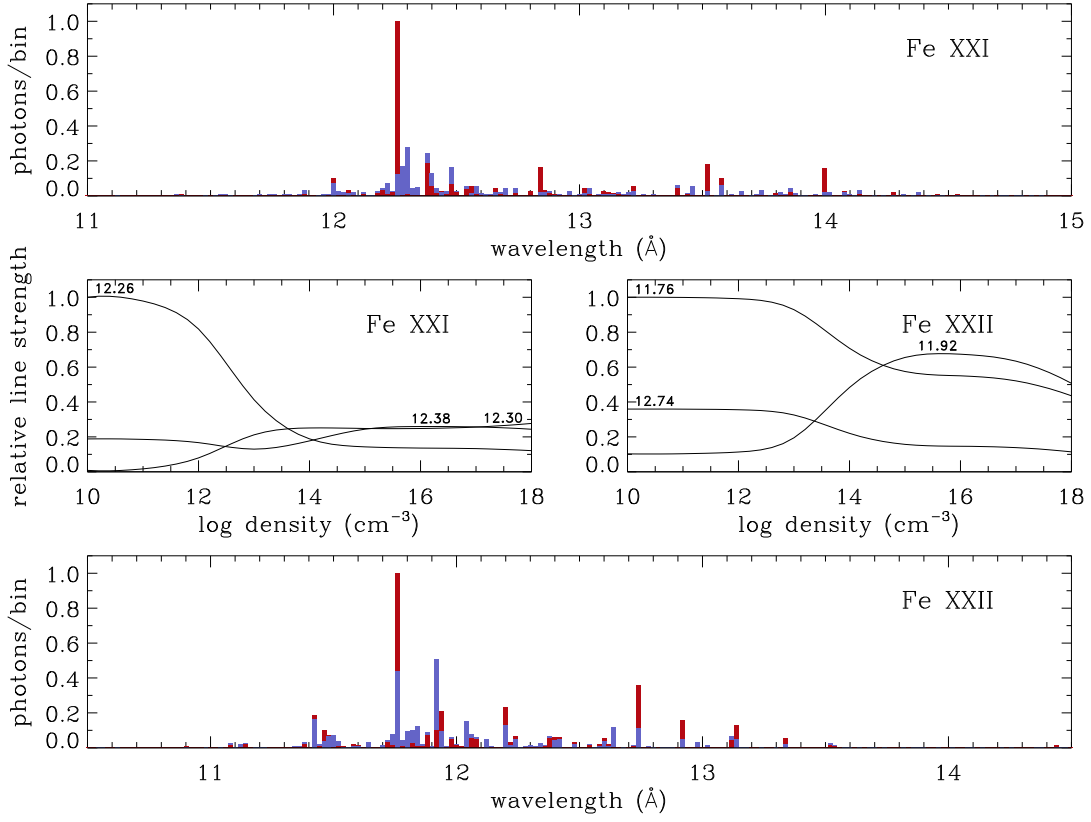


FIGURE 5. Similar to Fig 2, for Fe XXI at $T_e = 10.5$ MK and Fe XXII at $T_e = 12.3$ MK.

energy order, total angular momenta $J = 2, 1, 0$, and 1 . The $2p^6-2p^53s$ ($J = 0$) transition is strictly forbidden, but the remaining three levels $J = 2, 1$, and 1 decay to ground, producing lines at $17.10, 17.05$, and 16.78 Å, respectively. The 17.10 Å line is produced by an M2 transition, but it is nevertheless bright because the upper level is populated efficiently by radiative cascades, and its radiative branching ratio to ground is 1.0 . Since the radiative decay rate of this transition is slow compared to the other $2p-3l$ lines, collisional depopulation sets in at lower densities. Thus, the intensity ratio of the 17.10 Å line to any of the other $2p-3l$ lines provides a density diagnostic, as was first pointed out by Klapisch et al. [23].

To investigate quantitatively the density and photoexcitation dependence of the Fe XVII $I(17.10 \text{ Å})/I(17.05 \text{ Å})$ line ratio, we calculated LXSS models for this ion for $T_e = 4.1$ MK, $n_e = 10^{10}-10^{18} \text{ cm}^{-3}$, and $T_{bb} = 0-60$ kK (for additional details, see [28]). Fig 8 shows the LXSS model $I(17.10 \text{ Å})/I(17.05 \text{ Å})$ line ratio, the *Chandra* MEG spectrum of EX Hya in the neighborhood of the Fe XVII $2p-3s$ lines, and the value and $1, 2$, and 3σ error envelopes of the measured $I(17.10 \text{ Å})/I(17.05 \text{ Å})$ line ratio. The calculation shows that the blackbody temperature must be $T_{bb} \gtrsim 60$ kK to drive the $I(17.10 \text{ Å})/I(17.05 \text{ Å})$ line ratio into the high-density limit, while the figure shows that, in EX Hya, $n_e \gtrsim 2 \times 10^{14} \text{ cm}^{-3}$ or $T_{bb} \gtrsim 50$ kK at the 3σ level.

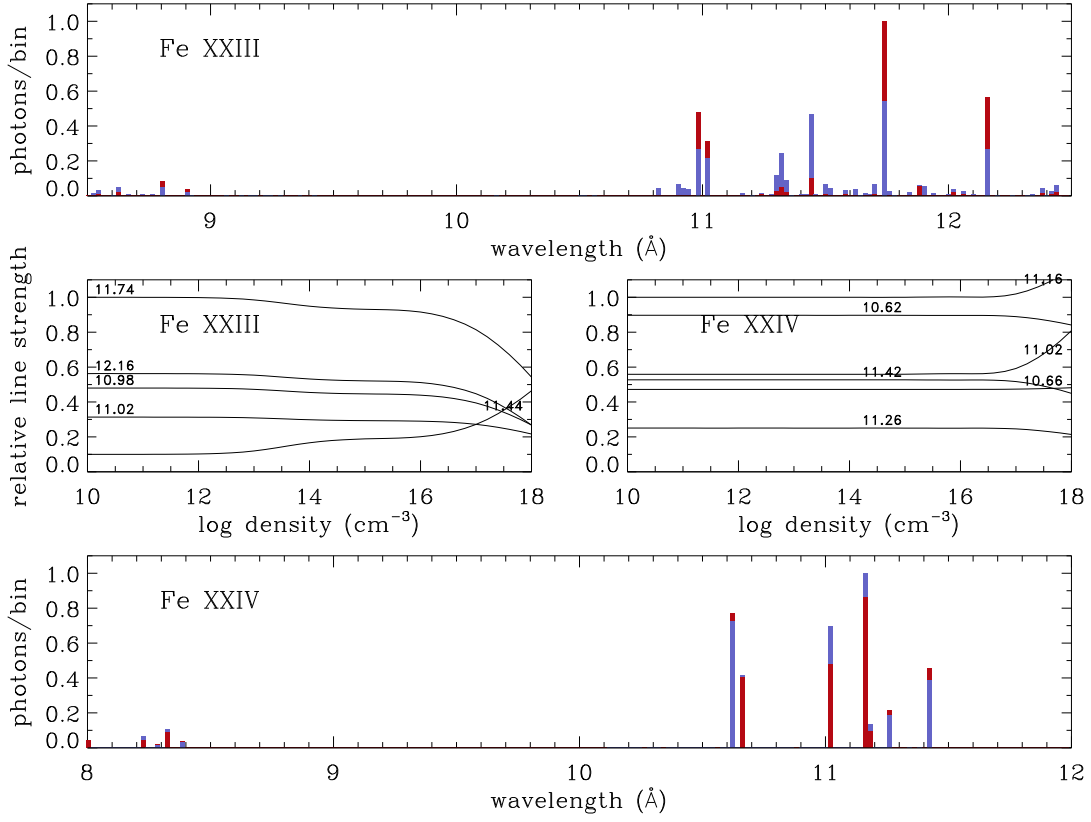


FIGURE 6. Similar to Fig 2, for Fe XXIII at $T_e = 14.1$ MK and Fe XXIV at $T_e = 17.8$ MK.

FE XXII

The density sensitivity of the X-ray lines of B-like Fe XXII has been discussed extensively in studies of the X-ray spectra of solar and laboratory high-temperature plasmas [9, 25, 8, 34, 11, 33, 42, 7]. At low densities, the Fe XXII electron population is primarily in the $2s^2 2p_{1/2}$ ground state, and collisional excitations are predominantly from the ground state into the $2s 2p^2$ manifold (8 levels) and the $2s^2 3d_{3/2}$ level, both of which decay primarily to ground, producing lines in the extreme ultraviolet (EUV) and at 11.77 \AA , respectively (Fig 7). However, these levels also decay to the $2s^2 2p_{3/2}$ first-excited level with approximately 15% probability, producing lines in the EUV and at 11.92 \AA ; when *that* level decays to ground, it produces a line in the ultraviolet. As the density increases, electron population builds up in the $2s^2 2p_{3/2}$ first-excited level because the M1 transition to ground is slow. At high densities, the $2s^2 2p_{3/2}$ first-excited level is fed primarily by radiative decays from the $2s 2p^2$ manifold. Collisional excitations out of the first-excited level are primarily into the $2s^2 3d_{5/2}$ level, which decays primarily back to the first-excited level, producing a line at 11.92 \AA . Consequently, the Fe XXII 11.92 \AA line is relatively strong in the X-ray spectra of high-density plasmas.

To investigate quantitatively the density and photoexcitation dependence of the

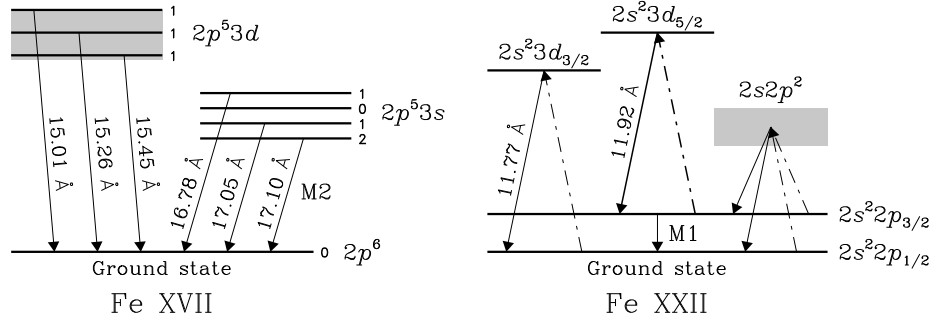


FIGURE 7. Simplified Grotrian diagrams for Fe XVII and Fe XXII. Collisional channels are shown with dot-dashed lines and radiative channels with solid lines; X-ray transitions are labeled with the wavelength.

Fe XXII $I(11.92 \text{ \AA})/I(11.77 \text{ \AA})$ line ratio, we calculated LXSS models for this ion for $T_e = 12.8 \text{ MK}$, $n_e = 10^{10} - 10^{18} \text{ cm}^{-3}$, and $T_{bb} = 0 - 100 \text{ kK}$. Motivated by the detailed study of Fournier et al. [14] of the density-sensitive Fe L-shell lines in the EUV, in these models we made two modifications to the collisional excitation data used in LXSS. First, we replaced, for all transitions between and among the $2s^2 2p$ and $2s 2p^2$ levels of Fe XXII, the electron impact excitation rate coefficients computed with HULLAC with those of Zhang & Pradhan [43] computed with the relativistic R-matrix method. Second, we added proton excitations for transitions among the levels of the $2s^2 2p$ and $2s 2p^2$ configuration using the proton impact excitation rate coefficients of Foster, Keenan, & Reid [13]. For additional details, see [29].

Fig 9 shows the resulting LXSS model $I(11.92 \text{ \AA})/I(11.77 \text{ \AA})$ line ratio, the *Chandra* MEG spectrum of EX Hya in the neighborhood of the Fe XXII $2p-3d$ lines, and the value and 1, 2, and 3 σ error envelopes of the measured $I(11.92 \text{ \AA})/I(11.77 \text{ \AA})$ line ratio. The figure shows that the $I(11.92 \text{ \AA})/I(11.77 \text{ \AA})$ line ratio is relatively insensitive to photoexcitation, and that, in EX Hya, $n_e = 1.0^{+2.0}_{-0.5} \times 10^{14} \text{ cm}^{-3}$ at the 1 σ level and $n_e \gtrsim 2 \times 10^{13} \text{ cm}^{-3}$ or $T_{bb} \gtrsim 100 \text{ kK}$ at the 3 σ level.

SUMMARY

We have provided a discussion of the density and photoexcitation sensitivity of the X-ray spectra of collisionally ionized Fe L-shell ions. Potentially useful density diagnostics are identified for Fe XVII and Fe XIX–Fe XXIII, with the most straightforward being the Fe XVII $I(17.10 \text{ \AA})/I(17.05 \text{ \AA})$ line ratio and the Fe XXII $I(11.92 \text{ \AA})/I(11.77 \text{ \AA})$ line ratio. Compared to the He-like R density diagnostics, the Fe L-shell density diagnostics are less sensitive to photoexcitation, hence are particularly valuable for sources like O stars and cataclysmic variables that are bright in the ultraviolet. Applying these models to the *Chandra* HETG spectrum of the intermediate polar EX Hya, we have shown that the observed Fe XVII $I(17.10 \text{ \AA})/I(17.05 \text{ \AA})$ line ratio is consistent with an electron density $n_e \gtrsim 2 \times 10^{14} \text{ cm}^{-3}$ (or a blackbody photoexcitation temperature $T_{bb} \gtrsim 50 \text{ kK}$) at the 3 σ level, while from the observed Fe XXII $I(11.92 \text{ \AA})/I(11.77 \text{ \AA})$

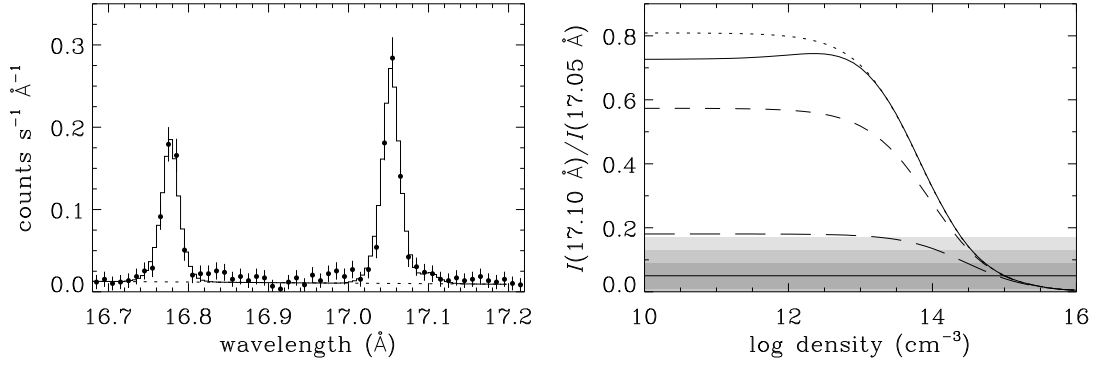


FIGURE 8. *Left panel:* Detail of the *Chandra* MEG spectrum of EX Hya in the neighborhood of the Fe XVII $2p$ – $3s$ lines. Data (combining ± 1 st orders and binned to 0.01 \AA) are shown by the filled circles with error bars and the model fit is shown by the histogram. *Right panel:* LXSS model Fe XVII $I(17.10 \text{ \AA})/I(17.05 \text{ \AA})$ line ratio as a function of electron density for $T_e = 4.1 \text{ MK}$ and $T_{bb} = 10, 30, 40,$ and 50 kK (solid, dotted, short dashed, and long dashed curves, respectively). Horizontal line and the dark, medium, and light shaded stripes indicate respectively the value and the 68%, 90%, and 99% confidence error envelopes of the line ratio measured in EX Hya.

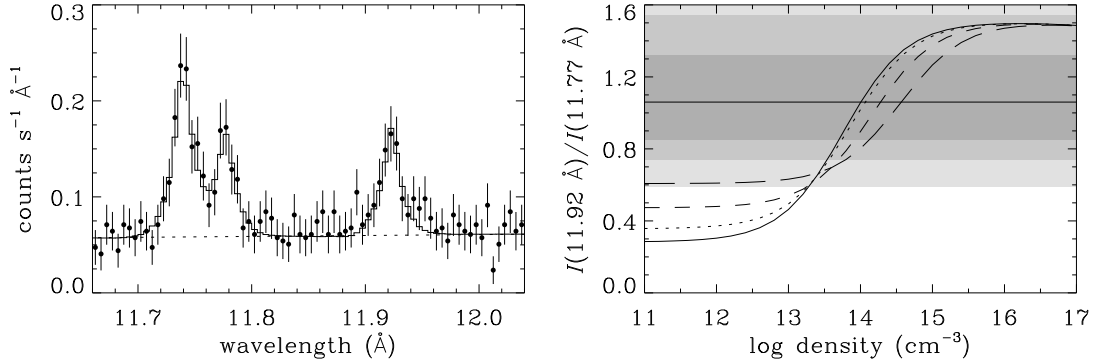


FIGURE 9. *Left panel:* Detail of the *Chandra* MEG spectrum of EX Hy in the neighborhood of the Fe XXII $2p$ – $3d$ lines. Data (combining ± 1 st orders and binned to 0.005 \AA) are shown by the filled circles with error bars and the model fit is shown by the histogram. *Right panel:* LXSS model Fe XXII $I(11.92 \text{ \AA})/I(11.77 \text{ \AA})$ line ratio as a function of electron density for $T_e = 12.8 \text{ MK}$ and $T_{bb} = 0, 60, 80,$ and 100 kK (solid, dotted, short dashed, and long dashed curves, respectively). Horizontal line and the dark, medium, and light shaded stripes indicate respectively the value and the 68%, 90%, and 99% confidence error envelopes of the line ratio measured in EX Hya.

line ratio, we infer $n_e = 1.0^{+2.0}_{-0.5} \times 10^{14} \text{ cm}^{-3}$ at the 1σ level and $n_e \gtrsim 2 \times 10^{13} \text{ cm}^{-3}$ (or $T_{bb} \gtrsim 100 \text{ kK}$) at the 3σ level. The high densities are assured in EX Hya, whose far ultraviolet spectrum has been modeled as a $T_{bb} \approx 25 \text{ kK}$ white dwarf [17] and as a $T_{bb} \approx 20 \text{ kK}$ white dwarf with a $T_{bb} \approx 37 \text{ kK}$ hotspot [26]. While these results are particular to EX Hya, the Fe L-shell density diagnostics are applicable to collisionally ionized laboratory (e.g., tokamak) or cosmic (e.g., cataclysmic variable) plasmas with electron temperatures $T_e \approx 2$ – 45 MK and electron densities $n_e \gtrsim 10^{11} \text{ cm}^{-3}$.

ACKNOWLEDGMENTS

We thank H. Tananbaum for the generous grant of Director's Discretionary Time that made possible the *Chandra* observations of EX Hya. Support for this work was provided in part by NASA through *Chandra* Award Number DD0-1004B issued by the *Chandra* X-Ray Observatory Center, which is operated by the Smithsonian Astrophysical Observatory for and on behalf of NASA under contract NAS8-39073. This work was performed under the auspices of the U.S. Department of Energy by University of California Lawrence Livermore National Laboratory under contract No. W-7405-Eng-48.

REFERENCES

1. Ayres, T. R., et al. 2001, *ApJ*, 549, 554
2. Bar-Shalom, A., Klapisch, M., & Oreg, J. 1988, *Phys. Rev. A*, 38, 1773
3. Beiersdorfer, P., von Goeler, S., Bitter, M., & Thorn, D. B. 2001, *Phys. Rev. A*, 64, 032705
4. Blumenthal, G. R., Drake, G. W. F., & Tucker, W. H. 1972, *ApJ*, 172, 205
5. Brickhouse, N. S., & Drake, J. J. 2000, *RevMexAA (Serie de Conferencias)*, 9, 24
6. Canizares, C. R., et al. 2000, *ApJ*, 539, L41
7. Chen, H., et al. 2004, *ApJ*, 611, 598
8. Doschek, G. A., Feldman, U., & Cowan, R. D. 1981, *ApJ*, 245, 315
9. Doschek, G. A., Meekins, J. F., & Cowan, R. D. 1973, *Sol. Phys.*, 29, 125
10. Eisenbart, S., Beuermann, K., Reinsch, K., & Gänsicke, B. T. 2002, *A&A*, 382, 984
11. Fawcett, B. C., Jordan, C., Lemen, J. R., & Phillips, K. J. H. 1987, *MNRAS*, 225, 1013
12. Frank, J., King, A., & Raine, D. 1992, *Accretion Power in Astrophysics* (Cambridge: CUP)
13. Foster, V. J., Keenan, F. P., & Reid, R. H. G. 1997, *At. Data Nucl. Data Tables*, 67, 99
14. Fournier, K. B., et al. 2001, *ApJ*, 561, 1144
15. Fujimoto, R., & Ishida, M. 1997, *ApJ*, 474, 774
16. Gabriel, A. H., & Jordan, C. 1969, *MNRAS*, 145, 241
17. Greeley, B. W., Blair, W. P., Long, K. S., & Knigge, C. 1997, *ApJ*, 488, 419
18. Hoogerwerf, R., Brickhouse, N. S., & Mauche, C. W. 2004, *ApJ*, 610, 411
19. Hurwitz, M., Sirk, M., Bowyer, S., & Ko, Y.-K. 1997, *ApJ*, 477, 390
20. Kahn, S. M., et al. 2001, *A&A*, 365, L312
21. Klapisch, M. 1971, *Computer Phys. Comm.*, 2, 239
22. Klapisch, M., Schwob, J., Fraenkel, B., & Oreg, J. 1977, *J. Opt. Soc. Am.*, 67, 148
23. Klapisch, M., et al. 1978, *Phys. Letters*, 69A, 34
24. Loulergue, M., & Nussbaumer, H. 1973, *A&Ap*, 24, 209
25. Mason, H. E., & Storey, P. J. 1980, *MNRAS*, 191, 631
26. Mauche, C. W. 1999, *ApJ*, 520, 822.
27. Mauche, C. W. 2002, in *The Physics of Cataclysmic Variables and Related Objects*, ed. B. T. Gänsicke, K. Beuermann, & K. Reinsch (San Francisco: ASP), 113
28. Mauche, C. W., Liedahl, D. A., & Fournier, K. B. 2001, *ApJ*, 560, 992
29. Mauche, C. W., Liedahl, D. A., & Fournier, K. B. 2003, *ApJ*, 588, L101
30. Mazzotta, P., Mazzitelli, G., Colafrancesco, S., & Vittorio, N. 1998, *A&AS*, 133, 403
31. Ness, J.-U., et al. 2002, *A&Ap*, 394, 911
32. Osten, R. A., et al. 2004, *ApJS*, 153, 317
33. Phillips, K. J. H., Bhatia, A. K., Mason, H. E., & Zarro, D. M. 1996, *ApJ*, 466, 549
34. Phillips, K. J. H., et al. 1982, *ApJ*, 256, 774
35. Phillips, K. J. H., Greer, C. J., Bhatia, A. K., Coffey, I. H., Barnsley, R., & Keenan, F. P. 1997, *A&A*, 324, 381
36. Porquet, D., Mewe, R., Dubau, J., Raassen, A. J. J., & Kaastra, J. S. 2001, *A&A*, 376, 1113
37. Porquet, D. 2005, this volume
38. Rugge, H. R., & McKenzie, D. L. 1985, *ApJ*, 297, 338
39. Saba, J. L. R., Schmelz, J. T., Bhatia, A. K., & Strong, K. T. 1999, *ApJ*, 510, 1064

40. Waldron, W. L., & Cassinelli, J. P. 2001, ApJ, 548, L45
41. Warner, B. 1995, Cataclysmic Variable Stars (Cambridge: CUP)
42. Wargelin, B. J., Beiersdorfer, P., Liedahl, D. A., Kahn, S. M., & von Goeler, S. 1998, ApJ, 496, 1031
43. Zhang, H. L., & Pradhan, A. K., 1997, A&AS, 123, 575